

Synthetic gauge potentials for the dark state polaritons in atomic media

Yu-Hung Kuan,¹ Siang-Wei Shao,¹ I-Kang Liu,² Julius Ruseckas,^{3,4} Gediminas Juzeliūnas,⁴ Yu-Ju Lin,⁵ and Wen-Te Liao^{1,6,*}

¹Department of Physics, National Central University, Taoyuan City 32001, Taiwan

²Joint Quantum Centre Durham-Newcastle, School of Mathematics, Statistics and Physics, Newcastle University, Newcastle upon Tyne, NE1 7RU, United Kingdom

³Baltic Institute of Advanced Technology, Pilies g. 16-8, LT-01403, Vilnius, Lithuania

⁴Institute of Theoretical Physics and Astronomy, Vilnius University, Saulėtekio 3, LT-10257 Vilnius, Lithuania

⁵Institute of Atomic and Molecular Sciences, Academia Sinica, Taipei 10617, Taiwan

⁶Physics Division, National Center for Theoretical Sciences, Hsinchu 30013, Taiwan

(Dated: April 23, 2021)

The quest of utilizing neutral particles to simulate the behaviour of charged particles in a magnetic field makes the generation of artificial magnetic field of great interest. The previous and the only proposal for the production of synthetic magnetic field for the dark state polaritons in electromagnetically induced transparency invokes the mechanical rotation of a sample. Here, we put forward an optical scheme to generate effective gauge potentials for stationary-light polaritons. To demonstrate the capabilities of our approach, we present recipes for having dark state polaritons in degenerate Landau levels and in driven quantum harmonic oscillator. Our scheme paves a novel way towards the investigation of the bosonic analogue of the fractional quantum Hall effect by electromagnetically induced transparency.

Over the last decade a considerable progress has been made in emulating the synthetic gauge fields for ultracold atoms [1–7], photonic systems [8–13], and electric circuits [14]. Among the photonic systems a special role is played by slow [15–18] and stationary [19–22] light forming in atomic media due to the electromagnetically induced transparency (EIT) [23–27]. Such a light is composed of quasiparticles known as the dark state polaritons (DSPs) [16, 17, 20, 21] made predominantly of atomic excitations, so the DSPs can interact strongly via the atom-atom interaction [28–34]. This can facilitate creating of strongly correlated quantum states, including the fractional Hall states. Yet the DSPs are electrically neutral quasiparticles and thus are not subjected to the vector potential which provides the Lorentz force needed for the Hall effects. Up to now the only method considered for producing the synthetic gauge potential for the stationary light (stationary DSPs) involves rotation of the atomic medium [35], where a synthetic magnetic field is produced in the rotating frame. However, there are technical problems associated with synthetic fields in the rotating frame [36, 37], and it is therefore desirable to engineer gauge potentials in the static laboratory frame.

In this article, we show a possible optical method to engineer synthetic gauge potentials for stationary-light polaritons providing non-zero effective magnetic fields in the static laboratory frame. Therefore an EIT system of DSPs can be a simulator for a charged particle in a magnetic field, like ultracold atoms in the laser radiation [1–7, 38–40]. We show a recipe to construct environments for Landau levels and a driven quantum harmonic oscillator by engineering the synthetic vector and scalar potentials for stationary DSPs. The key ingredient of our idea is transferring the coupled Optical-Bloch equations (OBE) [16, 19, 22] for a two-dimensional three-level- Λ -type EIT system (see Fig. 1) to an electron-like Schrödinger equation for the dark-state polarization ρ_{21} (see supplemental information)

$$i\hbar \frac{\partial \rho_{21}}{\partial t} = \frac{(\hbar \nabla + \vec{A})^2}{2m} \rho_{21} + U \rho_{21} + i \left(\frac{\Gamma}{2\Delta_p} \right) \frac{\hbar^2}{2m} \nabla^2 \rho_{21}, \quad (1)$$

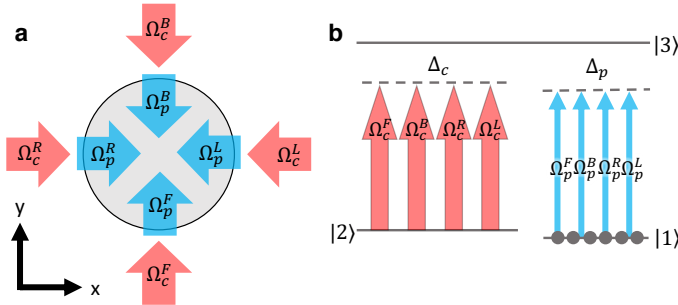


FIG. 1: **Two-dimensional EIT system.** **a**, The sketch for a two-dimensional EIT system. **b**, Three-level- Λ -type atomic system with two-photon detuning $\Delta_p - \Delta_c$. Red (blue)-upward arrows represent the control (probe) fields, and their label denotes the Rabi frequency.

with \hbar being the reduced Planck constant, where the synthetic vector potential \vec{A} , and scalar potential energy U read

$$\vec{A} = m\vec{V}_g, \quad (2)$$

$$U = \hbar(\Delta_p - \Delta_c) - \frac{1}{2m}|\vec{A}|^2. \quad (3)$$

The dark-state polarization ρ_{21} plays a role of the wavefunction, and the EIT group velocity $\vec{V}_g = (V_R - V_L, V_F - V_B, 0) = \frac{1}{2\eta} (|\Omega_c^R|^2 - |\Omega_c^L|^2, |\Omega_c^F|^2 - |\Omega_c^B|^2, 0)$ represents the vector potential \vec{A} for a unit charge. Here Δ_p (Δ_c) is the one-photon detuning of the probe (control) fields, Ω_c^F , Ω_c^B , Ω_c^R , and Ω_c^L are the Rabi frequencies of forward, backward, rightward and leftward propagating control fields, respectively, with the same total intensities for the pairs of the counterpropagating beams $\Omega_c^2 = |\Omega_c^R|^2 + |\Omega_c^L|^2 = |\Omega_c^F|^2 + |\Omega_c^B|^2$, $m = \frac{\hbar\eta^2}{2\Delta_p\Omega_c^2}$ is the effective mass when counter-propagating control fields are applied, $\eta = \frac{\Gamma\xi_x}{2L_x} = \frac{\Gamma\xi_y}{2L_y}$ is the light-matter coupling constant, Γ is the spontaneous decay rate of the excited state $|3\rangle$, and ξ_x (ξ_y) and L_x (L_y) are the optical depth and the medium length in the x (y) direction, respectively. In equation (7) the kinetic energy term dominates over the last diffusion term when $2\Delta_p \gg \Gamma$.

RESULTS

Landau levels. Given equations (7-9), one can simulate a charged particle moving in a background uniform magnetic field, especially the so-called Landau levels, in a two-dimensional EIT system. We manifest the generation of the synthetic \vec{A} of Landau gauge for the EIT dark state by preparing ρ_{21} in the n th Landau level $|n\rangle_L$ and then looking at its dynamics. Fig. 2a-c depict the time sequence (see supplemental information for the complete time sequence) used in our numerical simulations of the full set of OBE. First, in Fig. 2a the initial state is prepared by the typical EIT light storage technique [16, 17, 41, 42]. A resonant uniform forward control field and a weak co-propagating probe field with the transverse profile of the n th Landau level $\langle x|n\rangle_L$ and one-photon detuning $\Delta_p^s = -V_F k_s$ are injected into the medium along the y axis. By switching off the control field, the probe field is stored as the dark-state coherence in the medium

$$\rho_{21}(x, y) = \rho_0 H_n \left(\frac{x + k_s l_B^2}{l_B} \right) e^{ik_s y - \left(\frac{x + k_s l_B^2}{\sqrt{2}l_B} \right)^2}, \quad (4)$$

where H_n is the Hermite polynomial, and k_s is the longitudinal wavenumber of the slowly-varying amplitude. Subsequently four uniform control fields are turned on with a certain one photon detuning Δ_c , and the probe fields is retrieved under the two-photon resonance condition $\Delta_p = \Delta_c$ as depicted by Fig. 2b. This step endues ρ_{21} with an effective mass by the homogeneous detuning Δ_p . Finally, we switch on the required control fields with inhomogeneous detunings (gray-vertical double arrows) illustrated in Fig. 2c to build the Landau-gauge environment: $\Delta_c = \Delta_p - \frac{\Omega_c^2}{16\Delta_p L_x^2} x^2$, $\Omega_c^R = \Omega_c^L = \frac{\Omega_c}{\sqrt{2}}$, $\Omega_c^F = \frac{\Omega_c}{\sqrt{2}} \sqrt{1 + \frac{x}{L_x}}$, and $\Omega_c^B = \frac{\Omega_c}{\sqrt{2}} \sqrt{1 - \frac{x}{L_x}}$, which leads to $\vec{A} = \frac{\hbar\eta}{4L_x\Delta_p} (0, x, 0)$ and $U = 0$. The inhomogeneous Δ_c can be implemented by position-dependent Zeeman or Stark shifts to displace the atomic level $|2\rangle$ to $|2'\rangle$ [35, 40], as shown in Fig. 2c. Fig. 2d illustrates our two-dimensional Landau-gauge EIT system. The red-sinusoidal arrows denote the four control fields. The transversely gradient $\Omega_c^{F(B)}$ and the uniform $\Omega_c^{R(L)}$ are reflected by the density and opacity of arrows. Gray dots illustrate atoms, and the coloured density plot is the spatial profile of ρ_{21} . With above choices, the Landau levels are characterized by the magnetic length

$$l_B = \sqrt{\frac{8\Delta_p}{\xi_x\Gamma} L_x} = 2\sqrt{\frac{\Delta_p L_x}{\eta}}, \quad (5)$$

and the cyclotron frequency $\omega_B = \frac{\Omega_c^2}{\xi_x\Gamma}$. The dynamics of ρ_{21} on this stage is then governed by equation (7) giving three predictions: (i) $\rho_{21} = \langle x|n\rangle_L$ evolves with the angular frequency of $\omega_n = (n + 1/2)\omega_B$, (ii) the decay from Landau level $|n + 2\rangle_L$ to $|n\rangle_L$ takes place for $n \geq 2$ due to the last diffusion term (see supplemental information), and (iii) the strip-like wavefunction centers at $x = -k_s l_B^2$ and extends in the y direction.

Figure 3 demonstrates the first two predictions with $\Delta_p^s = 0$ and $k_s = 0$. In Fig. 3a gray-dashed lines depict the theoretical $\omega_n/\omega_B = (n + 1/2)$. The angular frequency of ρ_{21} is numerically calculated by $\omega_n = i(\partial_t \rho_{21})/\rho_{21}$ from our numerical solutions of OBE. The following EIT parameters are used: $\Gamma = 1\text{MHz}$, $\Delta_p = 0.83\Gamma$, $\Omega_c = 1.5\Gamma$, $\xi_x = 900$, $\xi_y = 800$, $L_x = 9\text{mm}$, and $L_y = 8\text{mm}$; this results in $m = 7 \times 10^{-32}\text{kg}$, $\omega_B = 2.5\text{kHz}$, and $l_B = 0.77\text{mm}$. Red-solid, green-solid, blue-solid, and orange-solid lines depict ω_n from our numerical solutions for $n = 0, 1, 2, 3$, respectively. In the beginning at $t = 0.44\text{ms}$ when the required control fields and detunings for Landau gauge EIT are chronologically switched on, there are four branches of the angular frequency, and each of the numerically calculated ω_n matches the theoretical prediction very well.

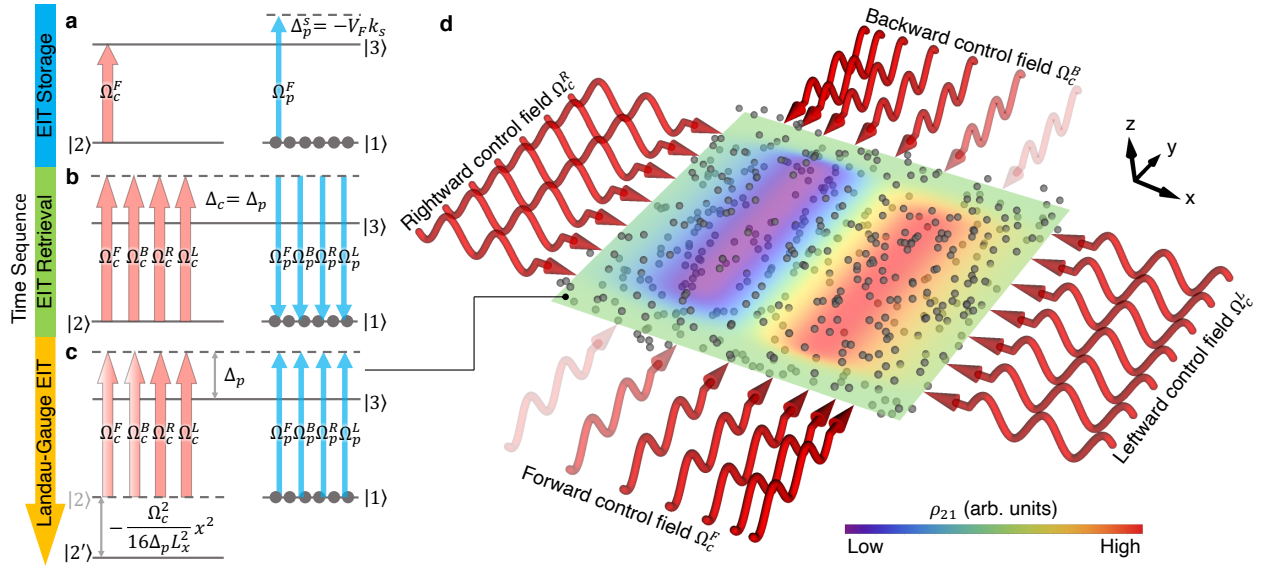


FIG. 2: **Landau-gauge EIT system and time sequence.** The time sequence is **a**, EIT light storage with probe one-photon detuning Δ_p^S , **b**, retrieval, and **c**, switching on the transversely gradient $\Omega_c^{F(B)}$ and the position-dependent two-photon detuning $\Delta_p - \Delta_c$. Red (blue)-upward arrows represent the control (probe) fields, and gray-vertical double arrows indicate detunings. **d**, The sketch for Landau-gauge EIT system. Gray dots represent atoms, and the red-sinusoidal arrows illustrate four control fields. The density and the opacity of arrows reflect the control field strength. The coloured density plot depicts the spatial distribution of the dark-state polarization ρ_{21} .

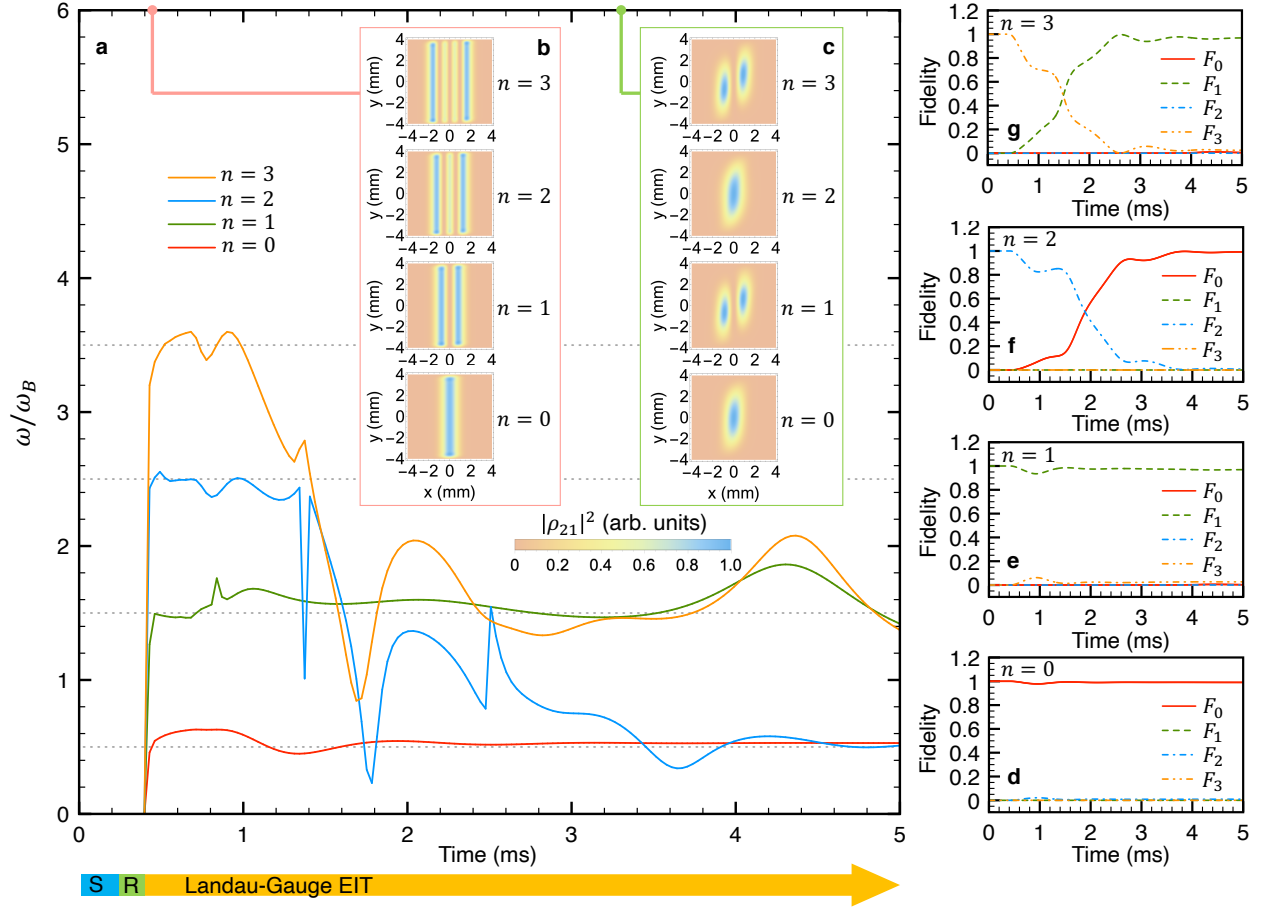


FIG. 3: **The evolution of Landau levels.** **a**, The evolution of the angular frequency of the EIT ground state coherence ρ_{21} initially prepared in the n th Landau level. Red-solid, green-solid, blue-solid, and orange-solid lines depict $n = 0, 1, 2, 3$, respectively. The bottom time arrow indicates different phases of the time sequence, where **S** and **R** indicate light storage and retrieval, respectively. The spatial profile of $|\rho_{21}|^2$ in different Landau levels at **b**, $t = 0.44$ ms when the Landau-gauge environment is switched on, and at **c**, $t = 3.3$ ms. The peak value of each $|\rho_{21}|^2$ is normalized to one. Fidelity for **d**, $n = 0$, **e**, $n = 1$, **f**, $n = 2$, and **g**, $n = 3$. Red-solid, green-dashed, blue-dashed-dotted, and orange-dashed-dotted-dotted lines illustrate F_0, F_1, F_2 , and F_3 , respectively.

Later on four branches converge in only two bands which manifests the prediction (ii) presented below Eq.(5). For a better visualization of the Landau-level evolution, Fig 3**b** demonstrates the spatial distribution of $|\rho_{21}|^2$ for a different input quantum number n at $t = 0.44\text{ms}$, and Fig 3**c** shows that at $t = 3.3\text{ms}$. One can observe that each Landau level $|n \geq 2\rangle_L$ gradually becomes $|n - 2\rangle_L$, but $|n < 2\rangle_L$ sustains. The longitudinal asymmetry is caused by the finite size effect of L_y . Moreover, we calculate the fidelity $F_{n'}(t) = |\langle n' | \rho_{21}(t) \rangle|^2 / \langle \rho_{21}(t) | \rho_{21}(t) \rangle$ to reveal the change of the projection of ρ_{21} on the n' th Landau level $|n'\rangle_L$. The evolution of the fidelity for input $n = 0, 1, 2$, and 3 is illustrated in **d**, **e**, **f**, and **g**, respectively. Remarkably, only $\Delta n = 2$ spontaneous transitions $|3\rangle_L \rightarrow |1\rangle_L$ and $|2\rangle_L \rightarrow |0\rangle_L$ show up in Fig. 3**f&g**, and $\Delta n = 1$ spontaneous decay is forbidden. This indicates the potential application of treating states $|1\rangle_L$ and $|0\rangle_L$ as a true and rather stable two-level system.

The prediction (iii) is one of the remarkable properties of the Landau level $\langle x - x_0 | n \rangle_L e^{ik_s y}$. One can test the Landau-gauge EIT via observing the x_0 -dependent motion of ρ_{21} for a given k_s . To prepare the initial state for the above purpose (see supplemental information for the complete time sequence), as depicted by Fig. 2**a**, one can store a probe field with the transverse profile $\langle x - x_0 | n \rangle_L$ centering on $x = x_0$ and non-zero $\Delta_p^s = -V_F k_s$. Figures 4**a-c** illustrate the stationary motion of $|\rho_{21}(x, y = 0, t)|^2$ for $k_s = \frac{2\pi}{L_y}, 0$ and $-\frac{2\pi}{L_y}$, respectively. Three wavenumbers are accordingly produced by $\Delta_p^s = -0.018\Gamma$, $\Delta_p^s = 0$, and $\Delta_p^s = 0.018\Gamma$. Our numerical solutions of OBE show the motional stability at their exact predicted peak position $x_0 = -k_s l_B^2$. The peak value of $|\rho_{21}(t)|^2$ is normalized to the unity for the sake of better visualization. On the other hand, having $x_0 \neq -k_s l_B^2$ causes a snake-like motion, as demonstrated in Figs. 4**d-f** for $k_s = \frac{2\pi}{L_y}, 0$ and $-\frac{2\pi}{L_y}$, respectively. This reflects the coherent state oscillation when the center of the Landau-gauge harmonic trap is shifted to $x = -k_s l_B^2$. Each non-stationary coherent state gradually decays to the ground state also due to the diffusion term in equation (7). The x_0 -dependent motion of the Landau level corresponds to the shifted harmonic potential and fulfils the prediction (iii) by equation (7). The dynamics of Landau levels reveals the effects of synthetic vector potential on the DSPs.

As a comparison with the mechanically rotating method [35], we estimate the magnetic length of two schemes. In the case of Eq. (5), when the transverse slope of the control fields approaches the diffraction limit, i.e., $L_x \approx \lambda$, and the kinetic energy term dominates over the diffusion one with the conservative choice of $\Delta_p = 10\Gamma$ in Eq. (7), we obtain the minimum $l_B = \frac{1}{\sqrt{\eta}} \sqrt{40\lambda\Gamma}$. In the rotating scheme one obtains the magnetic length $l_B^{\text{rot}} = \sqrt{\frac{\lambda}{4\pi} \frac{V_g}{\nu}} = \frac{1}{\sqrt{\eta}} \sqrt{\frac{\lambda\Omega_c^2}{8\pi\nu}}$, where V_g is the EIT slow light group velocity and ν the sample rotating angular frequency. The following typical values $\nu = 1\text{kHz} = 10^{-3}\Gamma$ and $\Omega_c = 1\Gamma$ also result in $l_B^{\text{rot}} = \frac{1}{\sqrt{\eta}} \sqrt{40\lambda\Gamma}$. Accordingly, our optical scheme can generate a synthetic magnetic field similar to that obtained by the rotation of a sample. The degeneracy of the lowest Landau level (LLL) is $D_{\text{lll}} = \frac{L_x L_y}{2\pi l_B^2}$, and the filling factor is $\nu_{\text{filling}} = 2\pi n_D l_B^2$, where n_D is the concentration of two-dimensional DSPs [35]. Given above estimation $l_B \geq \frac{1}{\sqrt{\eta}} \sqrt{40\lambda\Gamma}$, we

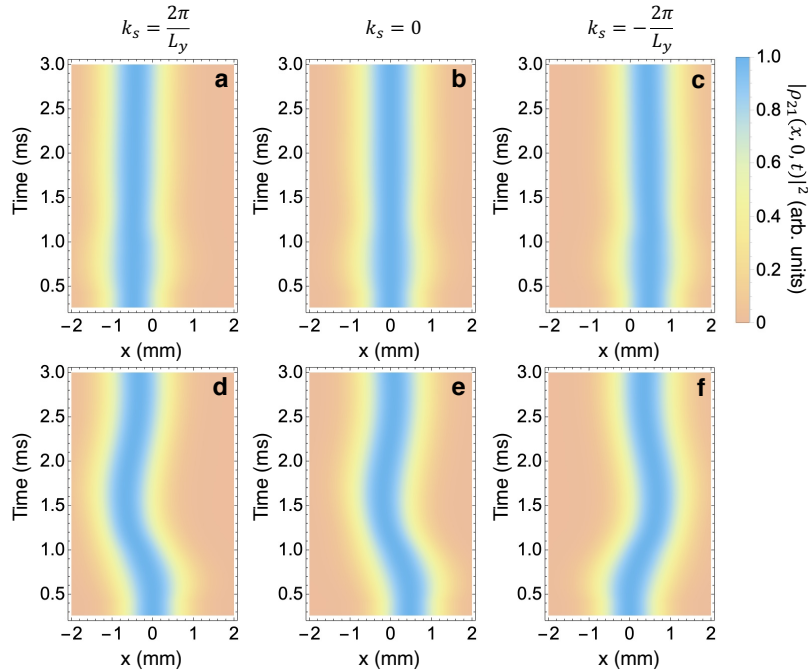


FIG. 4: **x_0 -dependent motion of Landau levels.** The motion of $|\rho_{21}(x, 0, t)|^2$ for **a**, $(k_s, x_0) = \left(\frac{2\pi}{L_y}, -kl_B^2\right)$, **b**, $(k_s, x_0) = (0, 0)$, **c**, $(k_s, x_0) = \left(-\frac{2\pi}{L_y}, kl_B^2\right)$, **d**, $(k_s, x_0) = \left(\frac{2\pi}{L_y}, 0\right)$, **e**, $(k_s, x_0) = (0, kl_B^2)$, and **f**, $(k_s, x_0) = \left(-\frac{2\pi}{L_y}, 0\right)$. The peak value of $|\rho_{21}(t)|^2$ is normalized to one.

obtain two conditions $D_{ll} \leq \frac{L_x L_y \eta}{80\pi\lambda\Gamma}$ and $\nu_{\text{filling}} \geq \frac{80\pi n_D \lambda \Gamma}{\eta}$. With the set of parameters used in Fig. 3 and $\lambda = 500\text{nm}$, one gets the maximum $D_{ll} = 2.9 \times 10^4$. A careful arrangement of the input probe photon distribution leads to $n_D = \frac{D_{ll}}{M L_x L_y} = \frac{\eta}{80M\pi\lambda\Gamma}$, where M can be some integer [43–45]. For $M > 1$ this results in a filling $\nu_{\text{filling}} = 1/M$ smaller than one. The vector potential \vec{A} can be also engineered in the symmetric gauge by introducing the gradients of the strength to four control fields.

Driven quantum harmonic oscillator. We now turn to simulate a driven quantum harmonic oscillator (QHO) with EIT by using synthetic stationary U and time-varying \vec{A} . When mimicking the driven QHO system, a time sequence similar to that shown in Figs. 2a-c can be utilized (see supplemental information for the complete time sequence). The initial state is prepared by storing a probe field with the profile of $\langle x|n\rangle_H$ where $|n\rangle_H$ is the n th eigenstate of QHO. This generates

$$\rho_{21}(x) = \rho_0 H_n \left(\frac{x}{l_E} \right) e^{-\left(\frac{x}{\sqrt{2}l_E} \right)^2} \quad (6)$$

in the medium. Afterwards, we turn on two counter-propagating control fields $\Omega_c^R = \Omega_c^L = \frac{\Omega_c}{\sqrt{2}}$ to retrieve a stationary pulse [19, 22, 46, 47] under the two-photon resonance condition $\Delta_c = \Delta_p$. Subsequently, we switch on the one-photon detuning $\Delta_c = \Delta_p - \frac{1}{2}\omega_E \left(\frac{x}{l_E} \right)^2 - \frac{2}{3}\beta\omega_E \left(\frac{x}{l_E} \right)^4$ depicted in the three-level scheme by Fig. 5a. On this stage ρ_{21} evolves as the n th QHO eigenstate in a harmonic trap under the quartic perturbation, namely, a synthetic $U = \frac{1}{2}m\omega_E^2 x^2 + \beta \frac{2m^2\omega_E^3}{3\hbar} x^4$ illustrated in Fig. 5b. The characteristic QHO length is given by $l_E = \frac{\Omega_c}{\xi_x \Gamma} \sqrt{\frac{8\Delta_p}{\omega_E}} L_x$. In view of equation (7), we can introduce $\Omega_c^R = \frac{\Omega_c}{\sqrt{2}} \sqrt{1 + \alpha \sin(\omega_d t)}$, and $\Omega_c^L = \frac{\Omega_c}{\sqrt{2}} \sqrt{1 - \alpha \sin(\omega_d t)}$ to construct $\vec{A} = \left(\alpha \frac{\hbar\eta}{4\Delta_p} \sin(\omega_d t), 0, 0 \right)$. The periodic modulation of the control fields shakes the dark-state polarization in a trapping potential U as demonstrated in Fig. 5c. Note that we are aiming at simulating the Hamiltonian neglecting the $|\vec{A}|^2$ term in Eqs. (7&9) as typically adopted in quantum optics, and so the two-photon detuning is not dynamically modulated. We derive the effective driving Rabi frequency $\Omega_A = \frac{1}{\hbar} \langle n+1 | \frac{\hbar e}{im} \vec{A} \cdot \nabla | n \rangle_H = \frac{\alpha\Omega_c}{4} \sqrt{\frac{(n+1)\omega_E}{\Delta_p}}$ and the perturbed eigen angular frequency $\omega_n = \left(n + \frac{1}{2} \right) \omega_E + \beta \left(n^2 + n + \frac{1}{2} \right) \omega_E$ for $\beta \ll 1$. The quartic

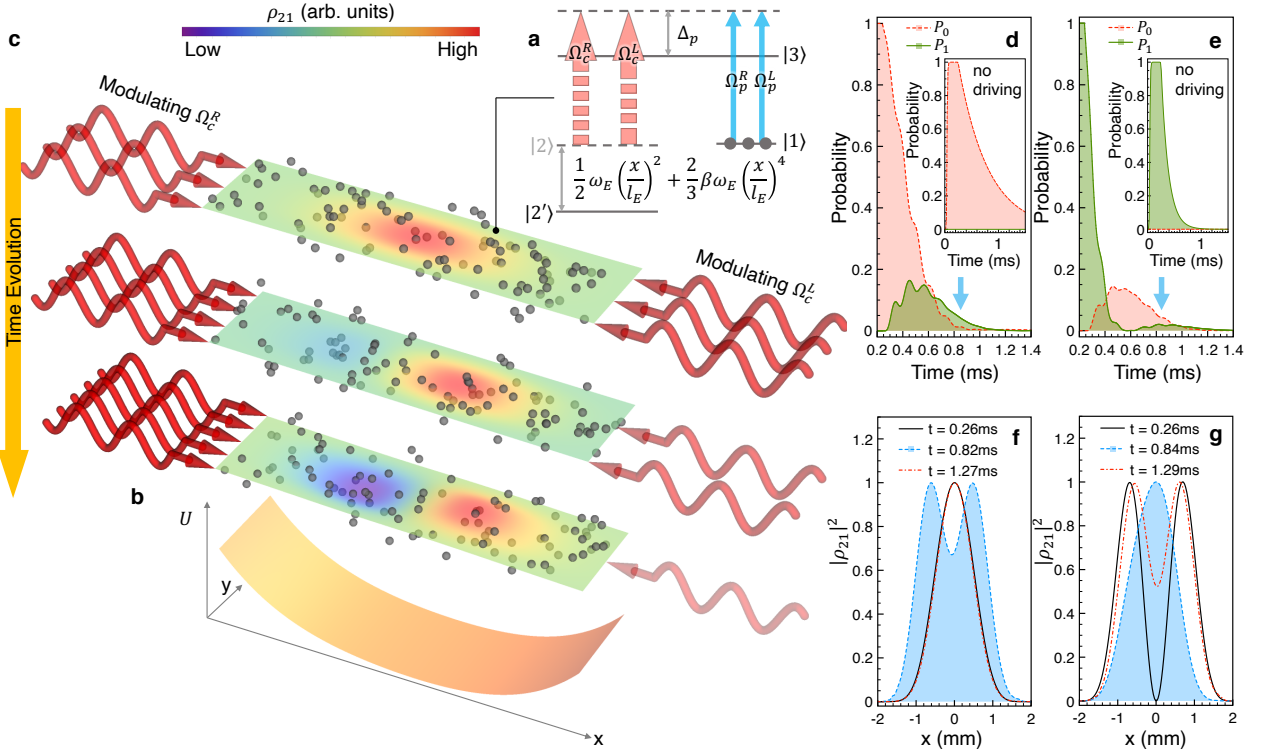


FIG. 5: **EIT simulator for a driven quantum harmonic oscillator.** **a**, Three-level EIT system. Blue-upward arrows depict the probe fields. The red-thick-dashed-upward arrows denote the periodically modulating Ω_c^R and Ω_c^L . The shifted level $|2'\rangle$ indicates the position-dependent two-photon detuning $\Delta_p - \Delta_c$. **b**, The x -dependent synthetic scalar potential energy U . **c**, The sketch of the EIT simulator for a driven QHO. Gray dots represent atoms, and the red-sinusoidal arrows illustrate two counter-propagating control fields. The density and the opacity of arrows reflect the control field strength. The coloured density plot depicts the profile of the coherence ρ_{21} . The evolution of the state probability $P_{n'}$ of the driven two-level system for initial states **d**, $|0\rangle$ and **e**, $|1\rangle$. Each inset is the result for a pair of static $\Omega_c^R = \Omega_c^L$. The snapshots of $|\rho_{21}(x, t)|^2$ for the driven transition **f**, $|0\rangle \rightarrow |1\rangle$ and **g**, $|1\rangle \rightarrow |0\rangle$.

potential breaks the equal energy spacing between neighbouring QHO eigenstates and renders driving only a chosen dipole transition possible by matching $\omega_d = \omega_{n+1} - \omega_n$.

Fig. 5d-g depict our numerical results with the following EIT parameters: $\alpha = 0.24$, $\beta = 0.15$, $\omega_E = 20\text{rad}\cdot\text{kHz}$, $\omega_d = 26\text{rad}\cdot\text{kHz}$, $\Gamma = 1\text{MHz}$, $\Delta_p = 4.6\Gamma$, $\Omega_c = 1.5\Gamma$, $\xi_x = 800$, and $L_x = 8\text{mm}$, which lead to $m = 1.27 \times 10^{-32}\text{kg}$, $l_E = 0.644\text{mm}$, and $\Omega_A = 6\text{rad}\cdot\text{kHz}$ for the QHO $|0\rangle_H \rightarrow |1\rangle_H$ transition. We calculate the state probability $P_{n'}(t) = |\langle n' | \rho_{21}(t) \rangle|^2 / \langle \rho_{21}(t_0) | \rho_{21}(t_0) \rangle$, where the dynamical modulation of Ω_c^R is switched on at $t = t_0 = 0.26\text{ms}$ and show the case for initial state $\rho_{21}(x, t_0) = \langle x | 0 \rangle_H$ in Fig. 5d. It is clear to see that the occurrence of $|0\rangle_H \rightarrow |1\rangle_H$ transition as predicted by equation (7). P_0 takes about 0.65ms to drop from 1 to 0, and P_1 simultaneously grows. As a comparison, the inset shows the case without dynamical modulation. The free decay of P_0 and non-growth P_1 reflect the dissipation of the EIT system in state $|0\rangle_H$, and P_0 spends about 2ms to descend from 1 to 0. The coherently driven excitation rate is significantly greater than the free decay rate of state $|0\rangle_H$. Moreover, we show the stimulated deexcitation of $|1\rangle_H \rightarrow |0\rangle_H$ in Fig. 5e, where initial state $|1\rangle_H$ is prepared. Compared with the inset using a pair of static Ω_c^R and Ω_c^L , not only the speed-up deexcitation due to the dynamical modulation happens, but also the revival of the first excited state occurs at $t = 0.9\text{ms}$. The latter is the signature of the damped Rabi oscillation in strong coupling regime, i.e., $\Omega_A \geq$ the decay rates. In order to further visualize the strong coupling effect, we illustrate $|\rho_{21}|^2$ at $t = 0.26\text{ms}$, $t = 0.82\text{ms}$, and $t = 1.27\text{ms}$ for the initial state $|0\rangle_H$ in Fig. 5f. Also, we show $|\rho_{21}|^2$ at $t = 0.26\text{ms}$, $t = 0.84\text{ms}$, and $t = 1.29\text{ms}$ for the initial state $|1\rangle_H$ in Fig. 5g. The clear alternation between $|\langle x | 0 \rangle_H|^2$ and $|\langle x | 1 \rangle_H|^2$ reveals the strong coherent coupling between two states as predicted by equation (7). The oscillation period is very close to the theoretical prediction, e.g., the second instants indicated by blue downward arrows in Fig. 5d&e are near $0.26\text{ms} + \pi/\Omega_A \approx 0.78\text{ms}$.

DISCUSSION

We have put forward a possible optical method to generate synthetic gauge fields for neutral EIT DSPs. Our optical scheme can not only produce comparable artificial magnetic field to that by mechanical rotation [35] but also provides a versatile platform to simulate different Hamiltonians, e. g., the demonstrated QHO for DSPs. Moreover, highly degenerate Landau levels are expected to be prepared by carefully adjusting the distribution of the number of interacting DSPs among LLL strips. The above DSP's dynamics can be observed by the direct imaging technique [48] or by the retrieving of the probe fields at different directions like tomography. An optical depth over 1000 has been experimentally achieved [49, 50]. Our scheme is also novel for the investigation of controllable non-Hermitian quantum systems.

METHODS

The probe light propagating in four directions are simulated by matrix method which stems from the Crank-Nicolson method. The behavior of atoms is simulated by the fourth-order Runge-Kutta method. The size of each temporal grid is about $300ns$, and the spacial grid is about $0.1mm$.

ACKNOWLEDGEMENTS

This work is supported by the Ministry of Science and Technology, Taiwan (Grant No. MOST 107-2112-M-008-007-MY3, MOST 109-2639-M-007-002-ASP & MOST 106- 2112-M-018-005-MY3). I-K.L. was supported by the Quantera ERA-NET cofund project NAQUAS through the Engineering and Physical Science Research Council, Grant No. EP/R043434/1. G.J. and J.R. were also supported by the National Center for Theoretical Sciences, Taiwan.

AUTHOR CONTRIBUTIONS

Y.-H. K. programmed the computational code. Y.-H. K. and S.-W. S. performed the numerical calculations. W.-T. L. and I.-K. L. derived the physics model. W.-T. L., Y.-J. L., and G. J. conceived the idea W.-T. L., conducted the project. All the authors discussed the results and wrote the manuscript.

* Electronic address: wente.liao@g.ncu.edu.tw

[1] J. Dalibard, F. Gerbier, G. Juzeliūnas, and P. Öhberg, Rev. Mod. Phys. **83**, 1523 (2011).

- [2] N. Goldman, G. Juzeliūnas, P. Öhberg, and I. B. Spielman, *Rep. Progr. Phys.* **77**, 126401 (2014).
- [3] M. Lewenstein, S. Anna, and A. Verònica, *Ultracold Atoms in Optical Lattices: Simulating quantum many-body systems* (Oxford University Press, 2012).
- [4] N. Goldman, J. C. Budich, and P. Zoller, *Nature Physics* **12**, 639 (2016), URL <https://doi.org/10.1038/nphys3803>.
- [5] Y.-J. Lin and I. B. Spielman, *Journal of Physics B: Atomic, Molecular and Optical Physics* **49**, 183001 (2016), URL <https://doi.org/10.1088/0953-4075/49/18/183001>.
- [6] N. R. Cooper, J. Dalibard, and I. B. Spielman, *Rev. Mod. Phys.* **91**, 015005 (2019), URL <https://link.aps.org/doi/10.1103/RevModPhys.91.015005>.
- [7] V. Galitski, I. Spielman, and G. Juzeliūnas, *Phys. Today* **72**, 38 (2019).
- [8] D.-W. Wang, H. Cai, L. Yuan, S.-Y. Zhu, and R.-B. Liu, *Optica* **2**, 712 (2015), URL <http://www.osapublishing.org/optica/abstract.cfm?URI=optica-2-8-712>.
- [9] N. Schine, A. Ryou, A. Gromov, A. Sommer, and J. Simon, *Nature* **534**, 671 (2016).
- [10] S. Mukherjee, H. K. Chandrasekharan, P. Öhberg, N. Goldman, and R. R. Thomson, *Nature Communications* **9**, 4209 (2018), URL <https://doi.org/10.1038/s41467-018-06723-y>.
- [11] T. Ozawa, H. M. Price, A. Amo, N. Goldman, M. Hafezi, L. Lu, M. C. Rechtsman, D. Schuster, J. Simon, O. Zilberberg, et al., *Rev. Mod. Phys.* **91**, 015006 (2019), URL <https://link.aps.org/doi/10.1103/RevModPhys.91.015006>.
- [12] L. W. Clark, N. Schine, C. Baum, N. Jia, and J. Simon, *Nature* **582**, 41 (2020).
- [13] A. D'Errico, F. Cardano, M. Maffei, A. Dauphin, R. Barboza, C. Esposito, B. Piccirillo, M. Lewenstein, P. Massignan, and L. Marrucci, *Optica* **7**, 108 (2020), URL <http://www.osapublishing.org/optica/abstract.cfm?URI=optica-7-2-108>.
- [14] I. Carusotto, A. A. Houck, A. J. Kollár, P. Roushan, D. I. Schuster, and J. Simon, *Nature Physics* **16**, 268 (2020), URL <https://doi.org/10.1038/s41567-020-0815-y>.
- [15] L. V. Hau, S. E. Harris, Z. Dutton, and C. H. Behroozi, *Nature* **397**, 594 (1999).
- [16] M. Fleischhauer and M. D. Lukin, *Phys. Rev. Lett.* **84**, 5094 (2000), URL <https://link.aps.org/doi/10.1103/PhysRevLett.84.5094>.
- [17] G. Juzeliūnas and H. J. Carmichael, *Phys. Rev. A* **65**, 021601 (2002), URL <https://link.aps.org/doi/10.1103/PhysRevA.65.021601>.
- [18] A. S. Zibrov, A. B. Matsko, O. Kocharovskaya, Y. V. Rostovtsev, G. R. Welch, and M. O. Scully, *Phys. Rev. Lett.* **88**, 103601 (2002).
- [19] M. Bajcsy, A. S. Zibrov, and M. D. Lukin, *Nature* **426**, 638 (2003).
- [20] S. A. Moiseev and B. S. Ham, *Phys. Rev. A* **73**, 033812 (2006), URL <https://link.aps.org/doi/10.1103/PhysRevA.73.033812>.
- [21] F. E. Zimmer, J. Otterbach, R. G. Unanyan, B. W. Shore, and M. Fleischhauer, *Phys. Rev. A* **77**, 063823 (2008), URL <https://link.aps.org/doi/10.1103/PhysRevA.77.063823>.
- [22] Y.-W. Lin, W.-T. Liao, T. Peters, H.-C. Chou, J.-S. Wang, H.-W. Cho, P.-C. Kuan, and I. A. Yu, *Phys. Rev. Lett.* **102**, 213601 (2009), URL <https://link.aps.org/doi/10.1103/PhysRevLett.102.213601>.
- [23] E. Arimondo, *Prog. Opt.* **35**, 257 (1996).
- [24] S. E. Harris, *Phys. Today* **50**, 36 (1997).
- [25] M. D. Lukin, *Rev. Mod. Phys.* **75**, 457 (2003).
- [26] M. Fleischhauer, A. Imamoglu, and J. P. Marangos, *Rev. Mod. Phys.* **77**, 633 (2005).
- [27] N. V. Vitanov, A. A. Rangelov, B. W. Shore, and K. Bergmann, *Rev. Mod. Phys.* **89**, 015006 (2017), URL <https://link.aps.org/doi/10.1103/RevModPhys.89.015006>.
- [28] A. V. Gorshkov, J. Otterbach, M. Fleischhauer, T. Pohl, and M. D. Lukin, *Phys. Rev. Lett.* **107**, 133602 (2011), URL <https://link.aps.org/doi/10.1103/PhysRevLett.107.133602>.
- [29] D. Petrosyan, J. Otterbach, and M. Fleischhauer, *Phys. Rev. Lett.* **107**, 213601 (2011), URL <https://link.aps.org/doi/10.1103/PhysRevLett.107.213601>.
- [30] T. Peyronel, O. Firstenberg, Q.-Y. Liang, S. Hofferberth, A. V. Gorshkov, T. Pohl, M. D. Lukin, and V. Vuletić, *Nature* **488**, 57 (2012), URL <https://doi.org/10.1038/nature11361>.
- [31] J. D. Pritchard, K. J. Weatherill, and C. S. Adams, *NONLINEAR OPTICS USING COLD RYDBERG ATOMS* (WORLD SCIENTIFIC, 2012), vol. Volume 1, pp. 301–350, ISBN 978-981-4440-39-4, URL https://doi.org/10.1142/9789814440400_0008.
- [32] M. Gärtner, S. Whitlock, D. W. Schönleber, and J. Evers, *Phys. Rev. Lett.* **113**, 233002 (2014), URL <https://link.aps.org/doi/10.1103/PhysRevLett.113.233002>.
- [33] C. R. Murray and T. Pohl, *Phys. Rev. X* **7**, 031007 (2017), URL <https://link.aps.org/doi/10.1103/PhysRevX.7.031007>.
- [34] D. Roy, C. M. Wilson, and O. Firstenberg, *Rev. Mod. Phys.* **89**, 021001 (2017), URL <https://link.aps.org/doi/10.1103/RevModPhys.89.021001>.
- [35] J. Otterbach, J. Ruseckas, R. G. Unanyan, G. Juzeliūnas, and M. Fleischhauer, *Phys. Rev. Lett.* **104**, 033903 (2010), URL <https://link.aps.org/doi/10.1103/PhysRevLett.104.033903>.
- [36] P. C. Haljan, I. Coddington, P. Engels, and E. A. Cornell, *Phys. Rev. Lett.* **87**, 210403 (2001), URL <https://link.aps.org/doi/10.1103/PhysRevLett.87.210403>.
- [37] N. R. Cooper, *Advances in Physics* **57**, 539 (2008).
- [38] G. Juzeliūnas and P. Öhberg, *Phys. Rev. Lett.* **93**, 033602 (2004).
- [39] G. Juzeliūnas, J. Ruseckas, P. Öhberg, and M. Fleischhauer, *Phys. Rev. A* **73**, 025602 (2006).
- [40] Y.-J. Lin, R. L. Compton, K. Jiménez-García, J. V. Porto, and I. B. Spielman, *Nature* **462**, 628 (2009).
- [41] D. F. Phillips, A. Fleischhauer, A. Mair, R. L. Walsworth, and M. D. Lukin, *Phys. Rev. Lett.* **86**, 783 (2001).
- [42] C. Liu, Z. Dutton, C. H. Behroozi, and L. V. Hau, *Nature* **409**, 490 (2001).
- [43] A. S. Sørensen, E. Demler, and M. D. Lukin, *Phys. Rev. Lett.* **94**, 086803 (2005), URL <https://link.aps.org/doi/10.1103/>

PhysRevLett.94.086803.

- [44] M. Hafezi, A. S. Sørensen, E. Demler, and M. D. Lukin, Phys. Rev. A **76**, 023613 (2007), URL <https://link.aps.org/doi/10.1103/PhysRevA.76.023613>.
- [45] A. Sterdyniak, N. Regnault, and G. Möller, Phys. Rev. B **86**, 165314 (2012), URL <https://link.aps.org/doi/10.1103/PhysRevB.86.165314>.
- [46] J. L. Everett, G. T. Campbell, Y.-W. Cho, P. Vernaz-Gris, D. B. Higginbottom, O. Pinel, N. P. Robins, P. K. Lam, and B. C. Buchler, Nature Physics **13**, 68 (2017).
- [47] K.-K. Park, Y.-W. Cho, Y.-T. Chough, and Y.-H. Kim, Phys. Rev. X **8**, 021016 (2018), URL <https://link.aps.org/doi/10.1103/PhysRevX.8.021016>.
- [48] G. T. Campbell, Y.-W. Cho, J. Su, J. Everett, N. Robins, P. K. Lam, and B. Buchler, Quantum Science and Technology **2**, 034010 (2017).
- [49] F. Blatt, T. Halfmann, and T. Peters, Optics Letters **39**, 446 (2014).
- [50] Y.-F. Hsiao, P.-J. Tsai, H.-S. Chen, S.-X. Lin, C.-C. Hung, C.-H. Lee, Y.-H. Chen, Y.-F. Chen, I. A. Yu, and Y.-C. Chen, Phys. Rev. Lett. **120**, 183602 (2018), URL <https://link.aps.org/doi/10.1103/PhysRevLett.120.183602>.

SYNTHETIC GAUGE POTENTIALS FOR THE DARK STATE POLARITONS IN ATOMIC MEDIA: SUPPLEMENTAL INFORMATION

The detail of our derivations and the time sequences used in our numerical simulation are demonstrated. We begin with Maxwell-Schrödinger equation in perturbation region, namely, $|\Omega_c| \gg |\Omega_p|$ [1, 2] and follow the derivation from [3].

$$\frac{\partial \rho_{21}}{\partial t} = \frac{i}{2} \Omega_c^{F*} \rho_{31}^F + \frac{i}{2} \Omega_c^{B*} \rho_{31}^B + \frac{i}{2} \Omega_c^{R*} \rho_{31}^R + \frac{i}{2} \Omega_c^{L*} \rho_{31}^L + i(\Delta_c - \Delta_p) \rho_{21}, \quad (7)$$

and

$$\frac{\partial \rho_{31}^F}{\partial t} = \frac{i}{2} \Omega_p^F + \frac{i}{2} \Omega_c^F \rho_{21} - \left(\frac{\Gamma}{2} + i\Delta_p \right) \rho_{31}^F, \quad (8)$$

$$\frac{\partial \rho_{31}^B}{\partial t} = \frac{i}{2} \Omega_p^B + \frac{i}{2} \Omega_c^B \rho_{21} - \left(\frac{\Gamma}{2} + i\Delta_p \right) \rho_{31}^B, \quad (9)$$

$$\frac{\partial \rho_{31}^R}{\partial t} = \frac{i}{2} \Omega_p^R + \frac{i}{2} \Omega_c^R \rho_{21} - \left(\frac{\Gamma}{2} + i\Delta_p \right) \rho_{31}^R, \quad (10)$$

$$\frac{\partial \rho_{31}^L}{\partial t} = \frac{i}{2} \Omega_p^L + \frac{i}{2} \Omega_c^L \rho_{21} - \left(\frac{\Gamma}{2} + i\Delta_p \right) \rho_{31}^L, \quad (11)$$

and wave equations

$$\frac{1}{c} \frac{\partial \Omega_p^F}{\partial t} + \frac{\partial \Omega_p^F}{\partial y} = i\eta \rho_{31}^F + \frac{i}{2k} \nabla^2 \Omega_p^F, \quad (12)$$

$$\frac{1}{c} \frac{\partial \Omega_p^B}{\partial t} - \frac{\partial \Omega_p^B}{\partial y} = i\eta \rho_{31}^B + \frac{i}{2k} \nabla^2 \Omega_p^B, \quad (13)$$

$$\frac{1}{c} \frac{\partial \Omega_p^R}{\partial t} + \frac{\partial \Omega_p^R}{\partial x} = i\eta \rho_{31}^R + \frac{i}{2k} \nabla^2 \Omega_p^R, \quad (14)$$

$$\frac{1}{c} \frac{\partial \Omega_p^L}{\partial t} - \frac{\partial \Omega_p^L}{\partial x} = i\eta \rho_{31}^L + \frac{i}{2k} \nabla^2 \Omega_p^L. \quad (15)$$

Here $\Omega_c^{F(B,R,L)}$ is the Rabi frequency of forward (backward, rightward, leftward) control field, and $\Omega_p^{F(B,R,L)}$ is the Rabi frequency of forward (backward, rightward, leftward) probe field. ρ_{21} is the ground state coherence between state $|1\rangle$ and $|2\rangle$, and $\rho_{31}^{F(B,R,L)}$ is the coherence between state $|1\rangle$ and $|3\rangle$ for forward (backward, rightward, leftward) EIT configuration. Δ_c and Δ_p are the detuning of control field and that of probe laser, respectively.

The basic strategy of derivation is to express all terms of probe field by ρ_{21} under adiabatic condition. First, we neglect $\frac{\partial \rho_{21}}{\partial t}$

and $\frac{\partial \rho_{31}^{F(B,R,L)}}{\partial t}$ in Eq. (7-11) and then get

$$\rho_{21} = \frac{- (\Omega_c^{F*} \Omega_p^F + \Omega_c^{B*} \Omega_p^B + \Omega_c^{R*} \Omega_p^R + \Omega_c^{L*} \Omega_p^L)}{2 (\Delta_c - \Delta_p) (2\Delta_p - i\Gamma) + |\Omega_c^F|^2 + |\Omega_c^B|^2 + |\Omega_c^R|^2 + |\Omega_c^L|^2}, \quad (16)$$

$$\Omega_p^F = -\Omega_c^F \rho_{21} + (2\Delta_p - i\Gamma) \rho_{31}^F \sim - \left[1 + \left(\frac{2\Delta_p - i\Gamma}{i\eta} \right) \frac{\partial}{\partial y} \right] \Omega_c^F \rho_{21}, \quad (17)$$

$$\Omega_p^B = -\Omega_c^B \rho_{21} + (2\Delta_p - i\Gamma) \rho_{31}^B \sim - \left[1 - \left(\frac{2\Delta_p - i\Gamma}{i\eta} \right) \frac{\partial}{\partial y} \right] \Omega_c^B \rho_{21}, \quad (18)$$

$$\Omega_p^R = -\Omega_c^R \rho_{21} + (2\Delta_p - i\Gamma) \rho_{31}^R \sim - \left[1 + \left(\frac{2\Delta_p - i\Gamma}{i\eta} \right) \frac{\partial}{\partial x} \right] \Omega_c^R \rho_{21}, \quad (19)$$

$$\Omega_p^L = -\Omega_c^L \rho_{21} + (2\Delta_p - i\Gamma) \rho_{31}^L \sim - \left[1 - \left(\frac{2\Delta_p - i\Gamma}{i\eta} \right) \frac{\partial}{\partial x} \right] \Omega_c^L \rho_{21}. \quad (20)$$

In order to get the last term in Eq.(17-20), we invoke $|\Omega_c^{F(B,R,L)} \rho_{21}| \gg |(2\Delta_p - i\Gamma) \rho_{31}^{F(B,R,L)}|$ and neglecting time derivative and ∇^2 in Eq. (12-15). Equation (7) also leads to

$$\Omega_c^{F*} \rho_{31}^F + \Omega_c^{B*} \rho_{31}^B + \Omega_c^{R*} \rho_{31}^R + \Omega_c^{L*} \rho_{31}^L = \frac{2}{i} \left[\frac{\partial}{\partial t} - i (\Delta_c - \Delta_p) \right] \rho_{21} \quad (21)$$

By doing $\Omega_c^{F*} \times \text{Eq. (12)} + \Omega_c^{B*} \times \text{Eq. (13)} + \Omega_c^{R*} \times \text{Eq. (14)} + \Omega_c^{L*} \times \text{Eq. (15)}$, one gets

$$\begin{aligned} & \frac{1}{c} \frac{\partial (\Omega_c^{F*} \Omega_p^F + \Omega_c^{B*} \Omega_p^B + \Omega_c^{R*} \Omega_p^R + \Omega_c^{L*} \Omega_p^L)}{\partial t} \\ & + \Omega_c^{F*} \frac{\partial \Omega_p^F}{\partial y} - \Omega_c^{B*} \frac{\partial \Omega_p^B}{\partial y} + \Omega_c^{R*} \frac{\partial \Omega_p^R}{\partial x} - \Omega_c^{L*} \frac{\partial \Omega_p^L}{\partial x} \\ & = i\eta (\Omega_c^{F*} \rho_{31}^F + \Omega_c^{B*} \rho_{31}^B + \Omega_c^{R*} \rho_{31}^R + \Omega_c^{L*} \rho_{31}^L) \\ & + \frac{i}{2k} (\Omega_c^{F*} \nabla^2 \Omega_p^F + \Omega_c^{B*} \nabla^2 \Omega_p^B + \Omega_c^{R*} \nabla^2 \Omega_p^R + \Omega_c^{L*} \nabla^2 \Omega_p^L). \end{aligned} \quad (22)$$

when $\Omega_c^{F(B,R,L)*} \frac{\partial \Omega_p^{F(B,R,L)}}{\partial t} \approx \frac{\partial [\Omega_c^{F(B,R,L)*} \Omega_p^{F(B,R,L)}]}{\partial t}$. We substitute Eq.(16-21) into Eq. (22) and get

$$\begin{aligned} & - \left[1 + \frac{V}{c} + \frac{(\Delta_c - \Delta_p) (2\Delta_p - i\Gamma)}{\eta c} \right] \frac{\partial \rho_{21}}{\partial t} + i (\Delta_c - \Delta_p) \rho_{21} \\ & = \vec{V}_g \cdot \nabla \rho_{21} + \frac{1}{2} (\nabla \cdot \vec{V}_g) \rho_{21} \\ & - \frac{\Gamma + 2i\Delta_p}{2\eta^2} \left[\Omega_c^{F*} \frac{\partial^2 (\Omega_c^F \rho_{21})}{\partial y^2} + \Omega_c^{B*} \frac{\partial^2 (\Omega_c^B \rho_{21})}{\partial y^2} + \Omega_c^{R*} \frac{\partial^2 (\Omega_c^R \rho_{21})}{\partial x^2} + \Omega_c^{L*} \frac{\partial^2 (\Omega_c^L \rho_{21})}{\partial x^2} \right] \\ & - \frac{i}{4k\eta} [\Omega_c^{F*} \nabla^2 (\Omega_c^F \rho_{21}) + \Omega_c^{B*} \nabla^2 (\Omega_c^B \rho_{21}) + \Omega_c^{R*} \nabla^2 (\Omega_c^R \rho_{21}) + \Omega_c^{L*} \nabla^2 (\Omega_c^L \rho_{21})] \\ & + \frac{i\Gamma - 2\Delta_p}{4k\eta^2} \left[\Omega_c^{F*} \nabla^2 \frac{\partial (\Omega_c^F \rho_{21})}{\partial y} - \Omega_c^{B*} \nabla^2 \frac{\partial (\Omega_c^B \rho_{21})}{\partial y} + \Omega_c^{R*} \nabla^2 \frac{\partial (\Omega_c^R \rho_{21})}{\partial x} - \Omega_c^{L*} \nabla^2 \frac{\partial (\Omega_c^L \rho_{21})}{\partial x} \right]. \end{aligned} \quad (23)$$

when the denominator of Eq. (16) is a constant. Here

$$V = \frac{|\Omega_c^R|^2 + |\Omega_c^L|^2 + |\Omega_c^F|^2 + |\Omega_c^B|^2}{2\eta} = V_R + V_L + V_F + V_B, \quad (24)$$

$$\vec{V}_g = \frac{1}{2\eta} (|\Omega_c^R|^2 - |\Omega_c^L|^2, |\Omega_c^F|^2 - |\Omega_c^B|^2, 0) = (V_R - V_L, V_F - V_B, 0). \quad (25)$$

Finally, we neglect (i) $\frac{V}{c} + \frac{(\Delta_c - \Delta_p)(2\Delta_p - i\Gamma)}{\eta c}$ in the first bracket and also (ii) last bracket where third derivative occurs in Eq. (23),

and arrive at

$$\begin{aligned}
i \frac{\partial \rho_{21}}{\partial t} &= -\frac{V}{2k} \nabla^2 \rho_{21} - \left(i \vec{V}_g + \frac{1}{2k} \nabla V \right) \cdot \nabla \rho_{21} - \frac{i}{2} \left(\nabla \cdot \vec{V}_g \right) \rho_{21} \\
&- \left(\frac{2\Delta_p - i\Gamma}{\eta} \right) \nabla \cdot \left[(V_R + V_L) \frac{\partial \rho_{21}}{\partial x}, (V_F + V_B) \frac{\partial \rho_{21}}{\partial y} \right] \\
&- \left[\Delta_c - \Delta_p + \frac{1}{4k\eta} \left(\Omega_c^{F*} \nabla^2 \Omega_c^F + \Omega_c^{B*} \nabla^2 \Omega_c^B + \Omega_c^{R*} \nabla^2 \Omega_c^R + \Omega_c^{L*} \nabla^2 \Omega_c^L \right) \right] \rho_{21} \\
&- \left(\frac{2\Delta_p - i\Gamma}{2\eta^2} \right) \left(\Omega_c^{F*} \frac{\partial^2 \Omega_c^F}{\partial y^2} + \Omega_c^{B*} \frac{\partial^2 \Omega_c^B}{\partial y^2} + \Omega_c^{R*} \frac{\partial^2 \Omega_c^R}{\partial x^2} + \Omega_c^{L*} \frac{\partial^2 \Omega_c^L}{\partial x^2} \right) \rho_{21}.
\end{aligned} \tag{26}$$

LANDAU GAUGE EIT

When $k \gg 1$ and

$$\Omega_c^R = \frac{\Omega_c}{\sqrt{2}}, \tag{27}$$

$$\Omega_c^L = \frac{\Omega_c}{\sqrt{2}}, \tag{28}$$

$$\Omega_c^F = \frac{\Omega_c}{\sqrt{2}} \sqrt{1 + \frac{x}{L_x}}, \tag{29}$$

$$\Omega_c^B = \frac{\Omega_c}{\sqrt{2}} \sqrt{1 - \frac{x}{L_x}}, \tag{30}$$

$$\Delta_c = \Delta_p - \frac{\Omega_c^2}{16\Delta_p L_x^2} x^2, \tag{31}$$

where Ω_c is some constant Rabi frequency, we get

$$V_R + V_L = \frac{\Omega_c^2}{2\eta}, \tag{32}$$

$$V_F + V_B = \frac{\Omega_c^2}{2\eta}, \tag{33}$$

$$\vec{V}_g = \frac{\Omega_c^2}{2\eta L_x} (0, x, 0), \tag{34}$$

and Eq. (26) becomes

$$\begin{aligned}
i \frac{\partial \rho_{21}}{\partial t} &= - \left(\frac{\Omega_c^2 \Delta_p}{\eta^2} \right) \nabla^2 \rho_{21} - i \frac{\Omega_c^2}{2\eta L_x} (0, -x) \cdot \nabla \rho_{21} + \frac{\Omega_c^2}{16\Delta_p L_x^2} x^2 \rho_{21}, \\
&= \left[\left(-i \frac{\Omega_c \sqrt{\Delta_p}}{\eta} \frac{\partial}{\partial x} \right)^2 + \left(-i \frac{\Omega_c \sqrt{\Delta_p}}{\eta} \frac{\partial}{\partial y} + \frac{\Omega_c}{4L \sqrt{\Delta_p}} x \right)^2 \right] \rho_{21} \\
&+ i\Gamma \left(\frac{\Omega_c^2}{2\eta^2} \right) \nabla^2 \rho_{21}.
\end{aligned} \tag{35}$$

Multiplying both side with \hbar , Eq. (35) becomes an electron-like Schrödinger equation:

$$\begin{aligned}
i\hbar \frac{\partial \rho_{21}}{\partial t} &= \frac{\Omega_c^2 \Delta_p}{\hbar \eta^2} \left[\left(\frac{\hbar}{i} \frac{\partial}{\partial x} \right)^2 + \left(\frac{\hbar}{i} \frac{\partial}{\partial y} + \frac{\hbar \eta}{4L_x \Delta_p} x \right)^2 \right] \rho_{21} \\
&+ i\hbar \Gamma \left(\frac{\Omega_c^2}{2\eta^2} \right) \nabla^2 \rho_{21} \\
&= \frac{(\hat{P} + e\vec{A})^2}{2m} \rho_{21} + i\hbar \Gamma \left(\frac{\Omega_c^2}{2\eta^2} \right) \nabla^2 \rho_{21}.
\end{aligned} \tag{36}$$

Here the effective wavefunction, momentum operator, effective vector potential, and effective mass are respectively

$$\psi = \rho_{21}, \quad (37)$$

$$\hat{P} = \frac{\hbar}{i} \nabla, \quad (38)$$

$$\vec{A} = \frac{\hbar\eta^2}{2e\Delta_p\Omega_c^2} \vec{V}_g = \frac{\hbar\eta}{4eL_x\Delta_p} (0, x, 0), \quad (39)$$

$$m = \frac{\hbar\eta^2}{2\Omega_c^2\Delta_p}. \quad (40)$$

One can then get the effective magnetic field

$$\vec{B} = \nabla \times \vec{A} = \frac{\hbar\eta}{4eL_x\Delta_p} (0, 0, 1), \quad (41)$$

the effective cyclotron frequency

$$\omega_B = \frac{e|\vec{B}|}{m} = \frac{\Omega_c^2}{2L_x\eta} = \frac{\Omega_c^2}{\xi_x\Gamma}, \quad (42)$$

and the effective magnetic length

$$l_B = \sqrt{\frac{\hbar}{e|\vec{B}|}} = 2\sqrt{\frac{L_x\Delta_p}{\eta}} = \sqrt{\frac{8\Delta_p}{\xi_x\Gamma}} L_x. \quad (43)$$

Non-Hermitian effect

We calculate the effect of the diffusion term in Eq. (36) in what follows

$$\begin{aligned} -i \left(\frac{\Gamma}{2\Delta_p} \right) \frac{1}{2m} \langle j | \hat{P}^2 | n \rangle &= \left(\frac{-i\Gamma}{4m\Delta_p} \right) \left(-\frac{m\hbar\omega_B}{2} \right) \langle j | (\hat{a}^+ - \hat{a})^2 | n \rangle \\ &= \left(\frac{i\Gamma\hbar\omega_B}{8\Delta_p} \right) \langle j | (\hat{a}^{+2} - \hat{a}^+\hat{a} - \hat{a}\hat{a}^+ + \hat{a}^2) | n \rangle \\ &= \left(\frac{i\Gamma\hbar\omega_B}{8\Delta_p} \right) [\langle j | (\hat{a}^{+2} + \hat{a}^2) | n \rangle - \langle n | (\hat{a}^+\hat{a} + \hat{a}\hat{a}^+) | n \rangle] \\ &= \left(\frac{i\Gamma\hbar\omega_B}{8\Delta_p} \right) [\sqrt{(n+1)(n+2)} \langle j | n+2 \rangle + \sqrt{n(n-1)} \langle j | n-2 \rangle - (2n+1) \langle j | n \rangle]. \end{aligned} \quad (44)$$

The first term indicates the $|n\rangle \rightarrow |n+2\rangle$ spontaneous transition, the second term depicts the $|n\rangle \rightarrow |n-2\rangle$ spontaneous decay, and the third term shows a dissipation of state $|n\rangle$. Note that the dissipation rate of state $|n+2\rangle$ is greater than the $|n\rangle \rightarrow |n+2\rangle$ spontaneous transition rate, and suppresses the latter. Above derivation shows the origin of $\Delta n = 2$ decay in Fig. 3.

Time sequence

The time sequences used in our numerical simulation of Eqs. (7-15) for Fig. 3 and Fig.4 are demonstrated in Fig. 6 and Fig. 7, respectively. The simulation box is in a two-dimensional domain of $-4.5\text{mm} \leq x \leq 4.5\text{mm}$ and $-4\text{mm} \leq y \leq 4\text{mm}$. The boundary condition at $y = -4\text{mm}$ is

$$\Omega_p^F(x, y = -4\text{mm}, t) = \Omega_0(t) H_n \left(\frac{x + kl_B^2}{l_B} \right) e^{-\left(\frac{x + kl_B^2}{\sqrt{2}l_B} \right)^2},$$

where $\Omega_0(t)$ is demonstrated in Fig. 6a and Fig. 7a. The $\Delta_p^s = 0.018\Gamma$ in Fig. 7b is for $k_s = -\frac{2\pi}{L_y}$ in Fig.4c&f. $\Delta_p^s = -0.018\Gamma$ and 0 are used for $k_s = \frac{2\pi}{L_y}$ and 0 in Fig.4, respectively. The Rabi frequency of control fields in Fig. 6c-f and Fig. 7c-f are given

by

$$\begin{aligned}
\Omega_c^F(x, t) &= \frac{\Omega_c}{2} \left[1 - \tanh\left(\frac{t-t_s}{\tau_s/4}\right) \right] \\
&\quad + \frac{\Omega_c}{2\sqrt{2}} \left[1 + \tanh\left(\frac{t-t_r}{\tau/4}\right) \right] \left\{ 1 + \left(-1 + \frac{\Omega_c}{\sqrt{2}} \sqrt{1 + \frac{x}{L_x}} \right) \frac{1}{2} \left[1 + \tanh\left(\frac{t-t_{LG}}{\tau/4}\right) \right] \right\}, \\
\Omega_c^B(x, t) &= \frac{\Omega_c}{2\sqrt{2}} \left[1 + \tanh\left(\frac{t-t_r}{\tau/4}\right) \right] \left\{ 1 + \left(-1 + \frac{\Omega_c}{\sqrt{2}} \sqrt{1 - \frac{x}{L_x}} \right) \frac{1}{2} \left[1 + \tanh\left(\frac{t-t_{LG}}{\tau/4}\right) \right] \right\}, \\
\Omega_c^R(x, t) &= \frac{\Omega_c}{2\sqrt{2}} \left[1 + \tanh\left(\frac{t-t_r}{\tau/4}\right) \right], \\
\Omega_c^L(x, t) &= \frac{\Omega_c}{2\sqrt{2}} \left[1 + \tanh\left(\frac{t-t_r}{\tau/4}\right) \right],
\end{aligned}$$

whose peak value is $\frac{\Omega_c}{\sqrt{2}} = \frac{1.5\Gamma}{\sqrt{2}} = 1.06\Gamma$. The detuning of control fields is

$$\Delta_c(x, t) = \frac{\Delta_p}{2} \left[1 + \tanh\left(\frac{t-t_r}{\tau/4}\right) \right] - \frac{\Omega_c^2}{16\Delta_p L_x^2} x^2 \frac{1}{2} \left[1 + \tanh\left(\frac{t-t_{LG}}{\tau/4}\right) \right].$$

Here $t_s = 0.4\text{ms}$, $t_r = 0.42\text{ms}$, $t_{LG} = 0.4225\text{ms}$, $\tau_s = 4\mu\text{s}$, and $\tau = 1\mu\text{s}$.

DRIVING QUANTUM HARMONIC OSCILLATOR

In order to simulate Rabi oscillation of a two-level quantum harmonic oscillator in a 1D EIT system, we introduce $\hat{P} \cdot \vec{A}$ Hamiltonian and perturbed quadratic potential by using

$$\Omega_c^R = \frac{\Omega_c}{\sqrt{2}} \sqrt{1 + \alpha \sin(\omega_d t)}, \tag{45}$$

$$\Omega_c^L = \frac{\Omega_c}{\sqrt{2}} \sqrt{1 - \alpha \sin(\omega_d t)}, \tag{46}$$

$$\Delta_c = \Delta_p - \frac{1}{2}\omega_E \left(\frac{x}{l_E}\right)^2 - \frac{2}{3}\beta\omega_E \left(\frac{x}{l_E}\right)^4 - \alpha^2 \frac{m\Omega_c^4}{8\hbar\eta^2} \sin^2(\omega_d t), \tag{47}$$

where the characteristic QHO length $l_E = \sqrt{\frac{\hbar}{m\omega_E}}$. We get

$$V_R + V_L = \frac{\Omega_c^2}{2\eta}, \tag{48}$$

$$\vec{V}_g = \left(\alpha \frac{\Omega_c^2}{2\eta} \sin(\omega_d t), 0, 0 \right), \tag{49}$$

and Eq. (26) becomes

$$\begin{aligned}
i \frac{\partial \rho_{21}}{\partial t} &= -\hbar \left(\frac{\Delta_p \Omega_c^2}{\hbar\eta^2} \right) \partial_x^2 \rho_{21} - i\alpha \frac{\Omega_c^2}{2\eta} \sin(\omega_d t) \partial_x \rho_{21} \\
&\quad + \left[\frac{1}{2\hbar} m\omega_E^2 x^2 + \beta \frac{2m^2\omega_E^3}{3\hbar^2} x^4 + \alpha^2 \frac{m\Omega_c^4}{8\hbar\eta^2} \sin^2(\omega_d t) \right] \rho_{21} + i\Gamma \left(\frac{\Omega_c^2}{2\eta^2} \right) \partial_x^2 \rho_{21} \\
&= \frac{1}{2m} \left[\hbar (-i\partial_x)^2 + 2m\alpha \frac{\Omega_c^2}{2\eta} \sin(\omega_d t) (-i\partial_x) + m^2\alpha^2 \frac{\Omega_c^4}{4\hbar\eta^2} \sin^2(\omega_d t) \right] \rho_{21} \\
&\quad + \left(\frac{1}{2\hbar} m\omega_E^2 x^2 + \beta \frac{2m^2\omega_E^3}{3\hbar^2} x^4 \right) \rho_{21} + i \frac{\hbar\Gamma}{2\Delta_p} \left(\frac{\Delta_p \Omega_c^2}{\hbar\eta^2} \right) \partial_x^2 \rho_{21}.
\end{aligned} \tag{50}$$

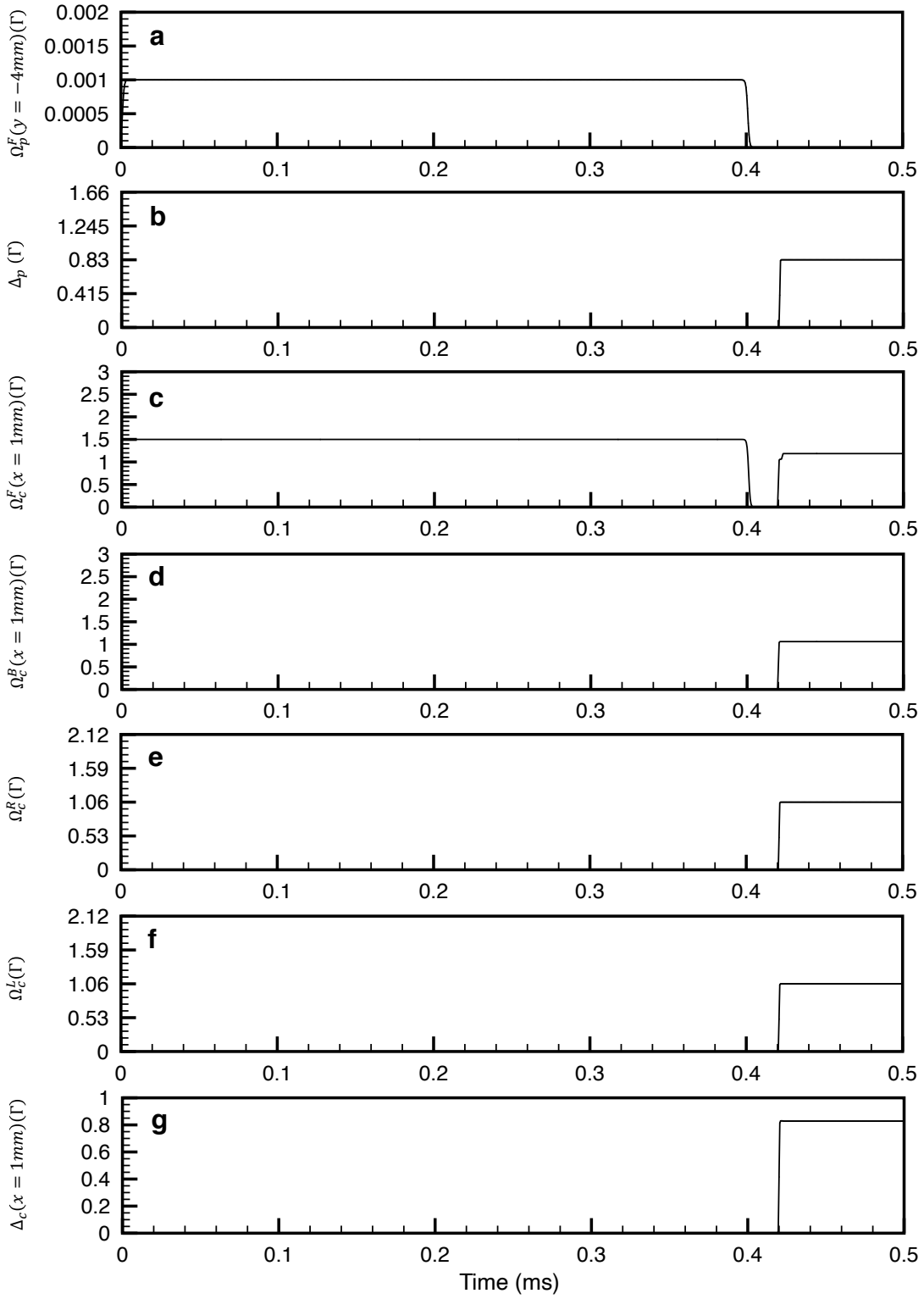


FIG. 6: **Time sequence for Landau-gauge EIT system Figure 3.** **a**, Input forward probe Rabi frequency Ω_p^F at $y = -4$ mm where is the input boundary of the medium. **b**, Probe detuning Δ_p for EIT light retrieval. **c**, Forward control Rabi frequency Ω_c^F for $x = 1$ mm. **d**, Backward control Rabi frequency Ω_c^B for $x = 1$ mm. **e**, Rightward control Rabi frequency Ω_c^R . **f**, Leftward control Rabi frequency Ω_c^L . **g**, Control detuning Δ_c for $x = 1$ mm.

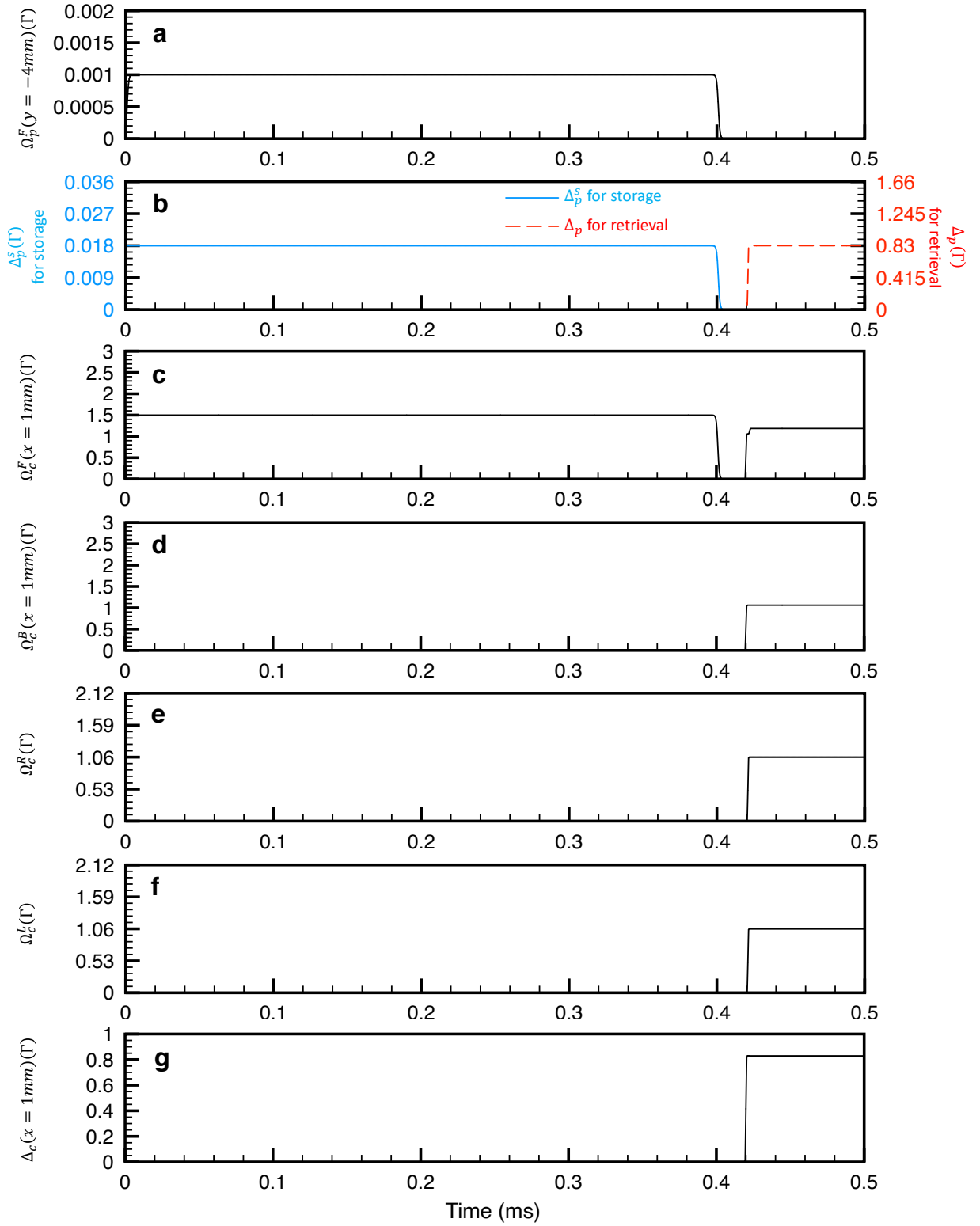


FIG. 7: **Time sequence for Landau-gauge EIT system** Figure 4. **a**, Input forward probe Rabi frequency Ω_p^F at $y = -4$ mm where is the input boundary of the medium. **b**, Probe detuning Δ_p^s and Δ_p are for EIT light storage (blue-solid line) and retrieval (red-dashed line), respectively. $\Delta_p^s = -0.018\Gamma$ is for Fig.4(a,d), $\Delta_p^s = 0$ for Fig.4(b,e), and $\Delta_p^s = 0.018\Gamma$ is for Fig.4(c,f). **c**, Forward control Rabi frequency Ω_c^F for $x = 1$ mm. **d**, Backward control Rabi frequency Ω_c^B for $x = 1$ mm. **e**, Rightward control Rabi frequency Ω_c^R . **f**, Leftward control Rabi frequency Ω_c^L . **g**, Control detuning Δ_c for $x = 1$ mm.

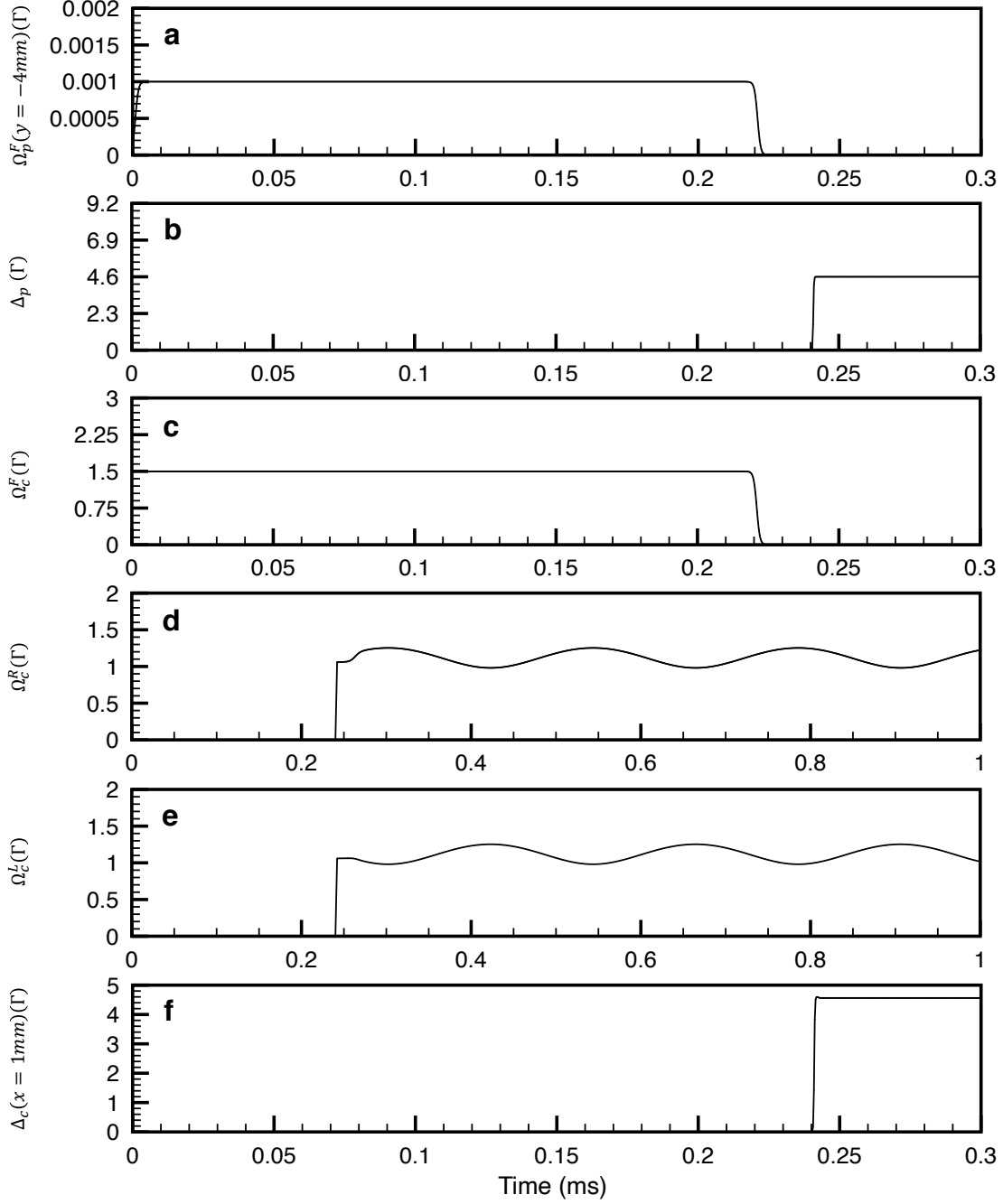


FIG. 8: **Time sequence for the driven QHO system Figure 5** **a**, Input forward probe Rabi frequency Ω_p^F at $y = -4\text{mm}$ where is the input boundary of the medium. **b**, Probe detuning Δ_p . **c**, Forward control Rabi frequency Ω_c^F . **d**, Rightward control Rabi frequency Ω_c^R . **e**, Leftward control Rabi frequency Ω_c^L . **f**, Control detuning Δ_c for $x = 1\text{mm}$.

Multiplying both side with \hbar , Eq. (50) becomes an electron-like Schrödinger equation:

$$\begin{aligned}
i\hbar \frac{\partial \rho_{21}}{\partial t} &= \frac{1}{2m} \left[(-i\hbar \partial_x)^2 + 2m\alpha \frac{\Omega_c^2}{2\eta} \sin(\omega_d t) (-i\hbar \partial_x) + \alpha^2 \frac{m^2 \Omega_c^4}{4\eta^2} \sin^2(\omega_d t) \right] \rho_{21} \\
&+ \left(\frac{1}{2} m \omega_E^2 x^2 + \beta \frac{2m^2 \omega_E^3}{3\hbar} x^4 \right) \rho_{21} - i \frac{\Gamma}{2\Delta_p} \left(\frac{1}{2m} \right) (-i\hbar \partial_x)^2 \rho_{21}. \\
&= \frac{1}{2m} \left\{ (-i\hbar \partial_x) + e \left[\alpha \frac{m \Omega_c^2}{2e\eta} \sin(\omega_d t) \right] \right\}^2 \rho_{21} \\
&+ \left(\frac{1}{2} m \omega_E^2 x^2 + \beta \frac{2m^2 \omega_E^3}{3\hbar} x^4 \right) \rho_{21} - i \frac{\Gamma}{2\Delta_p} \left(\frac{1}{2m} \right) (-i\hbar \partial_x)^2 \rho_{21}. \\
&= \frac{(\hat{P} + e\vec{A})^2}{2m} \rho_{21} + U \rho_{21} - i \left(\frac{\Gamma}{2\Delta_p} \right) \frac{\hat{P}^2}{2m} \rho_{21}. \tag{51}
\end{aligned}$$

Here the effective wavefunction, momentum operator, effective vector potential, and effective mass are respectively

$$\psi = \rho_{21}, \tag{52}$$

$$\hat{P} = \frac{\hbar}{i} \partial_x, \tag{53}$$

$$\vec{A} = \frac{\hbar \eta^2}{2e\Delta_p \Omega_c^2} \vec{V}_g = \left(\alpha \frac{\hbar \eta}{4e\Delta_p} \sin(\omega_d t), 0, 0 \right), \tag{54}$$

$$U = \frac{1}{2} m \omega_E^2 x^2 + \beta \frac{2m^2 \omega_E^3}{3\hbar} x^4, \tag{55}$$

$$m = \frac{\hbar \eta^2}{2\Omega_c^2 \Delta_p}. \tag{56}$$

One can then get the effective electric field and magnetic field

$$\vec{E} = -\nabla U - \frac{\partial \vec{A}}{\partial t} = \left(-m\omega_E^2 x - \beta \frac{8m^2 \omega_E^3}{3\hbar} x^3 - \alpha \frac{\hbar \eta \omega_d}{4e\Delta_p} \cos(\omega_d t), 0, 0 \right), \tag{57}$$

$$\vec{B} = \nabla \times \vec{A} = 0. \tag{58}$$

Driving Rabi frequency

We calculate the effective Rabi frequency $\Omega_A = \frac{e}{m\hbar} \vec{A} \cdot \hat{P}$ and neglect the small $|\vec{A}|^2$ term as typically adopted in quantum optics

$$\begin{aligned}
\Omega_A &= \frac{e}{m\hbar} \vec{A} \cdot \langle n+1 | \hat{P} | n \rangle = \frac{\alpha \eta}{4m\Delta_p} \sqrt{\frac{\hbar m \omega_E}{2}} \langle n+1 | (\hat{a}^+ - \hat{a}) | n \rangle = \frac{\alpha \eta}{4\Delta_p} \sqrt{\frac{\hbar \omega_E (n+1)}{2m}} \\
&= \frac{\alpha \Omega_c}{4} \sqrt{\frac{\omega_E (n+1)}{\Delta_p}}, \tag{59}
\end{aligned}$$

where \hat{a}^+ and \hat{a} are QHO raising and lowering operators, respectively. In the main text we use

$$\Delta_c = \Delta_p - \frac{1}{2} \omega_E \left(\frac{x}{l_E} \right)^2 - \frac{2}{3} \beta \omega_E \left(\frac{x}{l_E} \right)^4, \tag{60}$$

which also neglects the $|\vec{A}|^2$ term and leads to the same Rabi frequency.

The first-order perturbed eigen-energy

We invoke raising and lowering operators to calculate the first-order perturbed energy by the quartic term.

$$\begin{aligned}
\delta E_n^1 &= \beta \frac{2m^2 \omega_E^3}{3\hbar} \langle n | x^4 | n \rangle \\
&= \beta \frac{2m^2 \omega_E^3}{3\hbar} \left(\frac{\hbar}{2m\omega_E} \right)^2 \langle n | (\hat{a}^+ + \hat{a})^4 | n \rangle \\
&= \frac{\beta}{6} \hbar \omega_E \langle n | (\hat{a}^{+2} \hat{a}^2 + \hat{a}^+ \hat{a} \hat{a}^+ \hat{a} + \hat{a}^+ \hat{a}^2 \hat{a}^+ + \hat{a} \hat{a}^{+2} \hat{a} + \hat{a} \hat{a}^+ \hat{a} \hat{a}^+ + \hat{a}^2 \hat{a}^{+2}) | n \rangle \\
&= \beta \left(n^2 + n + \frac{1}{2} \right) \hbar \omega_E.
\end{aligned} \tag{61}$$

The first-order perturbed eigen energy under the quartic term reads

$$E_n = \left(n + \frac{1}{2} \right) \hbar \omega_E + \beta \left(n^2 + n + \frac{1}{2} \right) \hbar \omega_E. \tag{62}$$

Time sequence

The time sequences used in our numerical simulation of Eqs. (7-15) for Fig. 5 are demonstrated in Fig. 8. The simulation box is in a two-dimensional domain of $-4\text{mm} \leq x \leq 4\text{mm}$ and $-4\text{mm} \leq y \leq 4\text{mm}$. The boundary condition at $y = -4\text{mm}$ is

$$\Omega_p^F(x, y = -4\text{mm}, t) = \Omega_0(t) H_n \left(\frac{x}{l_E} \right) e^{-\left(\frac{x}{\sqrt{2}l_E} \right)^2},$$

where $\Omega_0(t)$ is demonstrated in Fig. 8a. The Rabi frequency of control fields in Fig. 8d&e are given by

$$\begin{aligned}
\Omega_c^F(x, t) &= \frac{\Omega_c}{2} \left[1 - \tanh \left(\frac{t - t_s}{\tau_s/4} \right) \right], \\
\Omega_c^R(x, t) &= \frac{\Omega_c}{2\sqrt{2}} \left[1 + \tanh \left(\frac{t - t_r}{\tau/4} \right) \right] \left\{ 1 + \left(-1 + \frac{\Omega_c}{\sqrt{2}} \sqrt{1 + \alpha \sin(\omega_d t)} \right) \frac{1}{2} \left[1 + \tanh \left(\frac{t - t_D}{\tau_D/4} \right) \right] \right\}, \\
\Omega_c^L(x, t) &= \frac{\Omega_c}{2\sqrt{2}} \left[1 + \tanh \left(\frac{t - t_r}{\tau/4} \right) \right] \left\{ 1 + \left(-1 + \frac{\Omega_c}{\sqrt{2}} \sqrt{1 - \alpha \sin(\omega_d t)} \right) \frac{1}{2} \left[1 + \tanh \left(\frac{t - t_D}{\tau_D/4} \right) \right] \right\},
\end{aligned}$$

whose peak value is $\frac{\Omega_c}{\sqrt{2}} = \frac{1.5\Gamma}{\sqrt{2}} = 1.06\Gamma$. The detuning of control fields is

$$\Delta_c(x, t) = \frac{\Delta_p}{2} \left[1 + \tanh \left(\frac{t - t_r}{\tau/4} \right) \right] - \left[\frac{1}{2} \omega_E \left(\frac{x}{l_E} \right)^2 + \frac{2}{3} \beta \omega_E \left(\frac{x}{l_E} \right)^4 \right] \frac{1}{2} \left[1 + \tanh \left(\frac{t - t_H}{\tau/4} \right) \right].$$

Here $t_s = 0.22\text{ms}$, $t_r = 0.241\text{ms}$, $t_H = 0.2425\text{ms}$, $t_D = 0.2625\text{ms}$, $\tau_s = 4\mu\text{s}$, $\tau = 1\mu\text{s}$, and $\tau_D = 25\mu\text{s}$.

* Electronic address: wente.liao@g.ncu.edu.tw

- [1] M. O. Scully and M. S. Zubairy, *Quantum Optics*, Cambridge University Press (2006).
[2] Yen-Wei Lin, Wen-Te Liao, Thorsten Peters, Hung-Chih Chou, Jian-Siung Wang, Hung-Wen Cho, and Pei-Chen Kuan, and Ite A Yu, Phys. Rev. Lett. **102**, 213601 (2009).
[3] M. Fleischhauer, and M. D. Lukin, Phys. Rev. Lett. **84**, 5094 (2000).